IUST
Iran University of
Science and Technology

Iranian Journal of Electrical and Electronic Engineering

Journal Homepage: ijeee.iust.ac.ir

Enhancing Misalignment Tolerance in Inductive Power Transfer System to Maintain Stable Power Transfer and Improve the Efficiency for Battery Charging

Mostafa Jalalian Ebrahimi *, M. A. Shamsi nejad ** (C.A.)

Abstract: This paper proposes an inductive power transfer (IPT) system to maintain stable power transfer and improve efficiency for battery charging performance across a wide range of coupling coefficient variations. The proposed IPT system uses series-series (*S-S*) and series-inductor-capacitor-inductor (*S-LCL*) compensation. In both compensation configurations, the rectifier operates in half-bridge (*HB*) and full-bridge (*FB*) modes. By using the correct switching pattern between compensation networks and the rectifier, four transfer power-coupling coefficient (*P-k*) curves are created. A 400 W prototype simulated in MATLAB demonstrates that, with the proposed method, output power fluctuation is limited to only 3% for coupling coefficients varying from 0.1 to 0.4, with system efficiency ranging from 80% to 95.9%. Compared to other methods, the proposed structure provides stable power transfer over an ultra-wide coupling variation and does not require special coil design, clamp circuit design, or complex control.

Keywords: Inductive Power Transfer (IPT), transfer power-coupling coefficient (*P-k*), Misalignment Tolerance, Power Fluctuation, Coupling Variation.

1 Introduction

IN recent years, inductive power transfer (IPT) systems have become a global research topic due to advantages such as electrical isolation, safety, power supply flexibility, and reliability [1]-[4]. IPT systems enable contactless energy transfer to a load through an air gap between the transmitter and receiver coils. Due to the lack of physical connections, IPT has been applied in many fields, such as electric vehicles, electric bicycles, biological implants, and consumer electronics [5]-[7]. Misalignment tolerance is a key indicator of IPT systems' flexibility and reliability, which has attracted significant research interest. Mobility, one of the most attractive properties, affects the relative position of the primary coil to the secondary coil. Therefore, misalignment between the primary and secondary coils is a common occurrence in IPT systems, usually in three directions: lateral, longitudinal, and vertical, causing mutual inductance to change over time. These changes lead to a change in the coupling coefficient of the system, which shifts the optimal operating point; thereby, the power fluctuation increases and reduces the efficiency of the system.

To reduce power fluctuation, a common method is coil design to achieve a uniform magnetic field against misalignment. To achieve this goal, various coil structures have been proposed, including double-D coils [8] and [9], bipolar coils [10], tripolar pads [11], three-coil structures [12], unsymmetrical coils [13], solenoid coils [14], and antiparallel windings [15]. These structures, by utilizing the flux cancellation approach between primary and secondary coils, can provide a nearly uniform coupling coefficient against misalignment. However, these solutions often face specific and stringent limitations and requirements, with most offering misalignment tolerance in only one or two directions.

Iranian Journal of Electrical & Electronic Engineering, YYYY.
Paper first received DD MONTH YYYY and accepted DD MONTH YYYY.

* The authors are with the Faculty of Electrical Engineering and Computer, University of Birjand, Birjand, South of Khorasan, Iran.
E-mails: M.Jalalian_e@birjand.ac.ir and mshamsi@birjand.ac.ir.
Corresponding Author: M. A.Shamsi-Nejad.

As an alternative solution, hybrid compensation networks have been proposed. In these topologies, by optimizing the compensation network parameters, stable power transfer can be achieved across a wide range of coupling coefficient variations [16]-[19]. Hybrid compensation networks are typically inductor-capacitor-capacitor/inductor-capacitor-capacitor (*LCC*/*LCC*) [17] and series/series (*S*/*S*) structures [20], or *LCC*/*S* [18] and *S*/*LCC* structures [21], aimed at achieving a wider range of coupling coefficient variations. Additionally, four-coil couplers have been introduced to enhance misalignment tolerance range [19]-[22]. Generally, these topologies demand precise coil design, additional or unique coils, numerous passive elements, complex control, and consequently, high production costs. Topologies such as *X*/*S* [23], *S*/*S* [24], *LCC*/*S* [25], and series/series-parallel (S/SP) [26] have been presented with carefully designed and optimized parameters for performance in the upper regions of the transfer power-coupling coefficient (*P*-*k*) curve, where power fluctuation exceeds 20% with 200% to 250% coupling variation. Therefore, despite the reduction in power fluctuation, expanding the misalignment tolerance range of these methods remains desirable. In these topologies, two compensation networks create two unique *P*-*k* curves that can expand the coupling coefficient range by switching between topologies. However, these methods suffer from high power fluctuation and reduced system efficiency due to loss of impedance matching conditions [27]-[29].

Some control methods have been introduced to tolerate changes in the coupling coefficient. To manage output power fluctuations, DC-DC converters, acting as active compensation networks on either the primary or secondary side, can adjust the output power against coupling coefficient variations through duty cycle tuning [30]. Additionally, using a variable inductor, controlled by the DC bias current, has been employed to manage power fluctuations and maintain output power stability against coupling factor changes [31]-[33]. In general, the disadvantages of these structures include core saturation, the need for real-time communication, precise design requirements for the variable inductor, increased weight, and compliance with electrical isolation and safety standards.

Recently, new approaches have been introduced to improve misalignment tolerance. In these methods, diode clamp circuits are employed for the automatic adaptability of each operating mode with coupling coefficient variations. Diode clamp circuits provide primary winding disconnection protection, soft start, and short circuit protection. These methods require the use of numerous active elements, auxiliary or additional coils, precise coupling identification, increased control complexity, and consequently, an escalation in total cost. Therefore, further investigation and development are needed for these methods to achieve simultaneous enhancements in efficiency and transfer power [34]-[39].

This paper proposes a detuned series-series/inductor-capacitor-inductor (*S*-*S*/*LCL*) compensated IPT system that extends the range of coupling variations to simultaneously achieve stable power transfer and relatively high efficiency. Compared to previous methods, the proposed approach does not require complex control or special coil design and demonstrates minimal output power fluctuations across a wide range of coupling coefficient variations. This paper is organized as follows: Section 2 presents the proposed detuned IPT topology. In Section 3, a 400 W sample of the proposed topology is simulated. Finally, comparisons and conclusions are provided in Sections 4 and 5, respectively.

2 Proposed Detuned IPT Topology

Fig. 1 shows an *S*-*S*/*LCL* compensation system for a wide range of coupling coefficient variations. The proposed structure consists of a dc voltage source, two relays (S_{w1} and S_{w2}), a high-frequency inverter with four MOSFETs (S_1- S_4), where V_{in} and V_o are the input and output dc voltages. U_{in} (U_o) and I_1 (I_2) represent the high-frequency input (output) voltage and current of the proposed topology.

The loosely coupled transformer consists of the primary coil L_1 and the secondary coil L_2, with M_{12} as the mutual inductance between the two coils. Capacitors C_1 (C_{21}, C_{22}, and C_{23}) are used to compensate for the inductance of the primary (secondary) coils, respectively. Three diodes (D_1- D_3), a MOSFET S_5, and the capacitor C_f form the output filter of the secondary rectifier. R_{ac} and R_L are the equivalent ac and dc loads, respectively.

When relays S_{w1} and S_{w2} are off, the system operates in detuned *S*-*S* mode; when relays S_{w1} and S_{w2} are on, the system operates in detuned *S*-*LCL* mode. Each of these two modes can also operate in half-bridge (*HB*) and full-bridge (*FB*) modes, i.e., *S*-*S*-*HB*, *S*-*LCL*-*FB*, *S*-*S*-*FB*, and *S*-*LCL*-*HB*, respectively. This topology ultimately creates four *P*-*k* curves that provide stable output power over a wide coupling range.

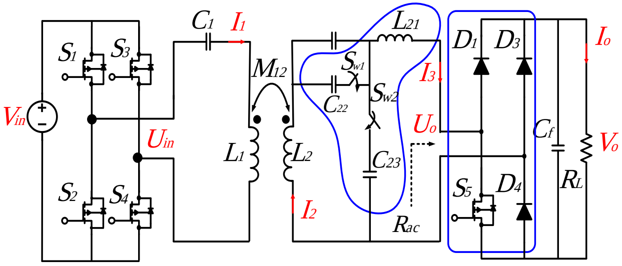

Fig. 1 an IPT system with *S*-*S*/*LCL* compensation topology.

2.1 Working principle of the detuned *S-S* mode

Fig. 2 shows the electrical equivalent circuit of the detuned *S-S* mode. In this mode, relays S_{w1} and S_{w2} are off, and the system operates in detuned *S-S* mode. The relationship between V_{in} and U_{in} can be expressed as follows:

$$V_{in} = \frac{\sqrt{2}\pi}{4} U_{in} \tag{1}$$

Fundamental harmonic approximation is used to analyze the system. According to Kirchhoff's voltage law, the detuned *S-S* mode in Fig. 2. can be expressed as follows:

$$\begin{bmatrix} U_{in} \\ 0 \end{bmatrix} = \begin{bmatrix} j(X_{L1} - X_{C1}) & -jX_{M12} \\ -jX_{M12} & j(X_{L2} - X_{C21} + X_{L21}) + R_{ac} \end{bmatrix} \begin{bmatrix} I_1 \\ I_2 \end{bmatrix}$$

Dis

Where

$$\begin{cases} X_{L1} = \omega L_1, X_{C1} = \dfrac{1}{\omega C_1}, M_{12} = k\sqrt{L_1 L_2}, X_{M_{12}} = \omega M_{12} \\ X_{L1} = \omega L_2, X_{L21} = \omega L_{21}, X_{C21} = \dfrac{1}{\omega C_{21}}, \omega = 2\pi f \end{cases}$$

f and *k* are the frequency of the inverter and the coupling coefficient, respectively.

R_L, $R_{ac\text{-}FB}$ and $R_{ac\text{-}HB}$ are the dc load, the ac load of the *FB* rectifier and the ac load of the *HB* rectifier, which are expressed as

$$R_{ac} = \begin{cases} R_{ac-FB} = \dfrac{8}{\pi^2} R_L \\ R_{ac-HB} = \dfrac{2}{\pi^2} R_L \end{cases} \rightarrow R_{ac-HB} = \frac{1}{4} R_{ac-FB} \tag{3}$$

In order to achieve a strong anti-misalignment capability and attain zero voltage switching (ZVS) of the inverter, the transmitter side is not in full resonance.

For this reason, in all working modes of the proposed structure, the ratio of detuning is considered:

$$\alpha = 1 - \frac{X_{C1}}{X_{L1}} \tag{4}$$

Where α is called the detuning ratio.

The input impedance Z_{in} and the corresponding phase angle θ_{in} in the detuned *S-S* mode are calculated as

$$\begin{cases} Z_{in} = \dfrac{X_{L1} X_{L2} k^2}{R_{ac}} + j\alpha X_{L1} \\ \theta_{in} = \tan^{-1}\left(\dfrac{\alpha R_{ac}}{X_{L2} k^2}\right) \end{cases} \tag{5}$$

To achieve maximum output power and increase system efficiency from the transmitter to the receiver in the detuned *S-S* mode, the secondary compensation must be in full resonance.

$$X_{L2} - X_{C21} + X_{L21} = 0 \tag{6}$$

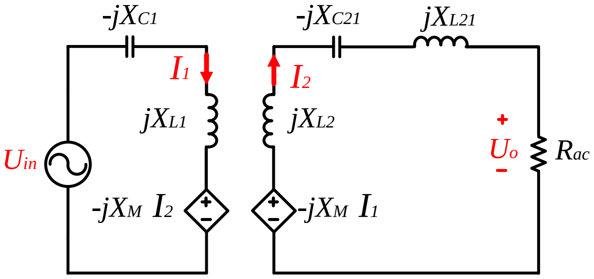

Fig. 2 equivalent circuit of detuned *S-S* mode.

Then, the output power P_{o1} of the detuned *S-S* mode can be expressed.

$$P_{o1} = R_{ac} \left| I_2 \right|^2 = \frac{R_{ac} X_{L1} X_{L2} k^2 U_{in}^2}{\alpha^2 X_{L1}^2 R_{ac}^2 + X_{L1}^2 X_{L2}^2 k^4} \tag{7}$$

According to (7), the output power can be considered a function of the coupling coefficient *k* (*0*<*k*<*1*), denoted as $P_{o1}(k)$. Fig. 3 illustrates the *P-k* curve in the detuned *S-S* mode. To calculate the coupling coefficient (k_{Pmax}) at the point of maximum output power, the derivative of P_{o1} (*k*) with respect to *k* is set equal to 0.

$$k_{P\max} = \sqrt{\frac{\alpha R_{ac}}{X_{L2}}} \tag{8}$$

By turning S_5 on and off, the detuned *S-S* topology switches from *S-S-HB* to *S-S-FB*, respectively. The *P-k* curve of the *S-S-FB* and *S-S-HB* modes under the same set of system parameters is shown in Fig. 4. Therefore, by inserting (3) into (8), the relationship between K_{Pmax1} and K_{Pmax3} can be obtained.

$$\begin{cases} k_{P\max 1} = \sqrt{\dfrac{2\alpha R_L}{\pi^2 X_{L2}}} \\ k_{P\max 3} = \sqrt{\dfrac{8\alpha R_L}{\pi^2 X_{L2}}} \end{cases} \rightarrow k_{P\max 3} = 2k_{P\max 1} \tag{9}$$

At the inflection point, the output power can reach its maximum value P_{max1}, which is

$$P_{\max-S-S}^{HB} = P_{\max-S-S}^{FB} = P_{\max 1} = \frac{U_{in}^2}{2\alpha X_{L1}} \tag{10}$$

According to (9), k_{Pmax3} is twice k_{Pmax1}. This means that the *P-k* curve in the *S-S-FB* mode is shifted to the right compared to the *P-k* curve in the *S-S-HB* mode under the same set of parameters.

In Fig. 4, it is clear that the hatched areas correspond to low output power. Therefore, the structure must be generalized and designed in a way that maintains the output power curve at its maximum (or near maximum) value over a wide range of coupling coefficient variations.

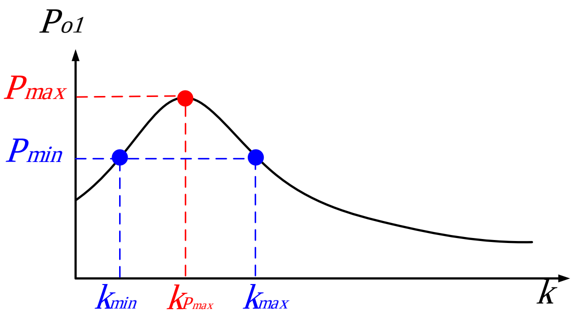

Fig. 3 the *P*-*k* curve of detuned *S*-*S* topology.

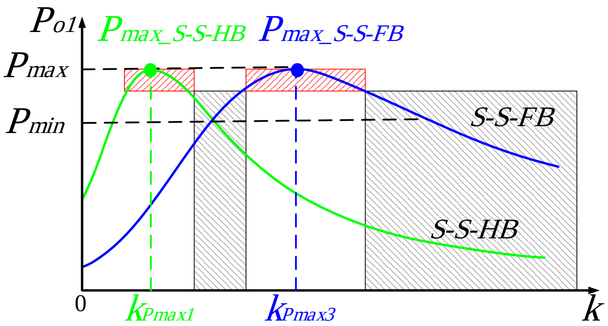

Fig. 4 the detuned *S*-*S* topology set in *FB* and *HB* modes.

2.2 Working principle of the detuned *S-LCL* mode

In order to simultaneously improve system efficiency and achieve maximum (or near-maximum) output power over a wide range of coupling coefficients, this compensation network is added to the secondary side of the detuned *S*-*S* structure. Fig. 5 shows the electrical equivalent circuit of the detuned *S*-*LCL* mode.

The relationships on this working mode can be expressed as.

$$\begin{bmatrix} U_{in} \\ 0 \\ 0 \end{bmatrix} = \begin{bmatrix} j(X_{L1}-X_{C1})+R_1 & -jX_{M12} & 0 \\ -jX_{M12} & j(X_{L2}-X'_{C2}-X_{C23})+R_{21} & jX_{C23} \\ 0 & jX_{C23} & j(X_{L21}-X_{C23})+R_{22}+R_{ac} \end{bmatrix} \begin{bmatrix} I_1 \\ I_2 \\ I_3 \end{bmatrix} \quad \textbf{Disp}$$

The input impedance Z_{in} and the corresponding phase angle θ_{in} in the detuned *S*-*LCL* mode are calculated as

$$\begin{cases} Z_{in} = \dfrac{X_{L1}X_{L2}R_{ac}k^2}{X_{C23}^2} + j\alpha X_{L1} \\ \theta_{in} = \tan^{-1}\left(\dfrac{\alpha X_{C23}^2}{X_{L2}R_{ac}k^2}\right) \end{cases} \tag{12}$$

To maximize the output power and increase efficiency from the transmitter side to the receiver side in the detuned *S*-*LCL* mode, the secondary compensator network should be in full resonance

$$\begin{aligned} X_{L2} - X'_{C2} - X_{C23} &= 0 \\ X_{L23} - X_{C23} &= 0 \end{aligned} \tag{13}$$

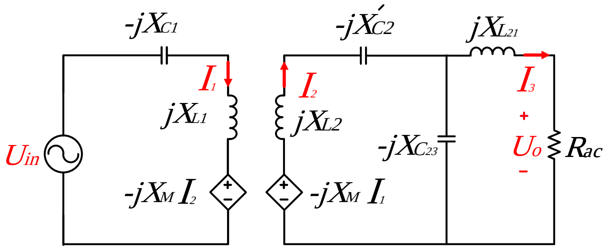

Fig. 5 equivalent circuit of detuned *S-LCL* mode.

By substituting (13) into (11), the transfer power in this mode is equal to

$$P_{o2} = R_{ac}\left|I_3\right|^2 = \frac{R_{ac}X_{L1}X_{L2}X_{C23}^2k^2U_{in}^2}{\alpha^2X_{L2}^2X_{C23}^4 + R_{ac}^2X_{L1}^2X_{L2}^2k^4} \quad \textbf{Disp}$$

In order to calculate the k_{Pmax} at the point of maximum output power, the derivative of $P_{o2}(k)$ with respect to k is set equal to 0.

$$k_{P\max} = \sqrt{\frac{\alpha}{R_{ac}X_{L2}}} \tag{15}$$

By turning S_5 off and on, the detuned *S*-*LCL* structure is changed from *S*-*LCL*-*FB* to *S*-*LCL*-*HB*, respectively. By inserting (3) into (15), the relationship between k_{Pmax2} and k_{Pmax4} can be obtained.

$$\begin{cases} k_{P\max 2} = \sqrt{\dfrac{\alpha\pi^2}{8R_L X_{L2}}} \\ k_{P\max 4} = \sqrt{\dfrac{\alpha\pi^2}{2R_L X_{L2}}} \end{cases} \rightarrow k_{P\max 4} = 2k_{P\max 2} \tag{16}$$

By substituting k_{Pmax2} and k_{Pmax4} in (14), the maximum output power is obtained in *S*-*LCL*-*FB* mode and *S*-*LCL*-*HB* mode.

$$P^{HB}_{\max-S-LCL} = P^{FB}_{\max-S-LCL} = P_{\max 2} = \frac{U_{in}^2}{2\alpha X_{L1}} \tag{17}$$

As seen, (10) and (17) are equal. Therefore, the maximum power (P_{max}) is the same in four working modes.

$$P_{\max 1} = P_{\max 2} = P_{\max} = \frac{U_{in}^2}{2\alpha X_{L1}} \tag{18}$$

It should be noted that the minimum power (P_{min}) in four working modes can be expressed as

$$P_{\min 1} = P_{\min 2} = P_{\min} \tag{19}$$

Fig. 6. illustrates the *P*-*k* curve of the detuned *S*-*LCL* structure in both *FB* and *HB* modes. By carefully designing the parameters of the secondary compensator network, the upper areas of the *P*-*k* curves in Fig. 6 are configured to fill the lower areas of the *P*-*k* curves in Fig. 5.

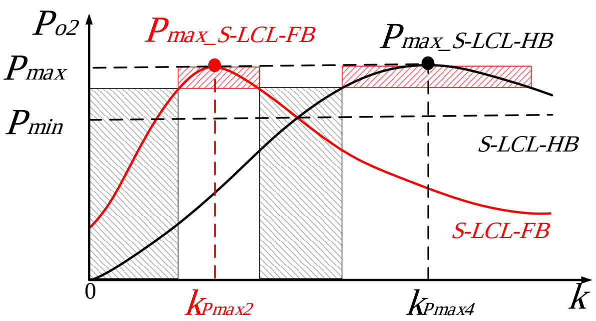

Fig. 6 the detuned *S-LCL* topology set in *FB* and *HB* modes.

Therefore, over a wide range of coupling coefficients, the output power can be maintained at the upper points of the curve.

2.3 Boundary coupling coefficient between modes

To reach the upper regions of the four *P-k* curves during changes in the coupling coefficient, it is essential to determine the boundary coupling coefficient between the modes of the proposed structure. According to (9) and (16), the switching intervals are *S-S-HB*, S-*LCL*-FB, *S-S-FB*, and then *S-LCL-HB*. To describe power fluctuations, a variable β is defined as:

$$\beta=\frac{P_{\max}-P_{\min}}{P_{\max}+P_{\min}} \tag{20}$$

Substituting (20) into (18) yields the P_{min} in terms of the power fluctuation coefficient:

$$P_{\min}=\frac{(1-\beta)}{(1+\beta)}P_{\max}=\frac{(1-\beta)}{(1+\beta)}\frac{U_{in}{}^{2}}{2\alpha X_{L1}} \tag{21}$$

The transition between working modes across the four curves is controlled by coupling coefficients. To determine the boundary regions for each operating mode, the intersection points of each curve must be calculated by equating the output power of the previous mode with that of the next mode.

$$P_{o1}=P_{o2}\rightarrow\begin{cases} k_{b1}=\sqrt{\dfrac{\alpha X_{C23}}{2X_{L2}}} \\ k_{b2}=\sqrt{\dfrac{\alpha X_{C23}}{X_{L2}}} \\ k_{b3}=\sqrt{\dfrac{2\alpha X_{C23}}{X_{L2}}} \end{cases} \tag{22}$$

In (22), k_{b1} represents the boundary coupling coefficient between *S-S-HB* mode and *S-LCL-FB* mode, k_{b2} represents the boundary coupling coefficient between *S-LCL-FB* mode and *S-S-FB* mode, and k_{b3} represents the boundary coupling coefficient between *S-S-FB* mode and *S-LCL-HB* mode.

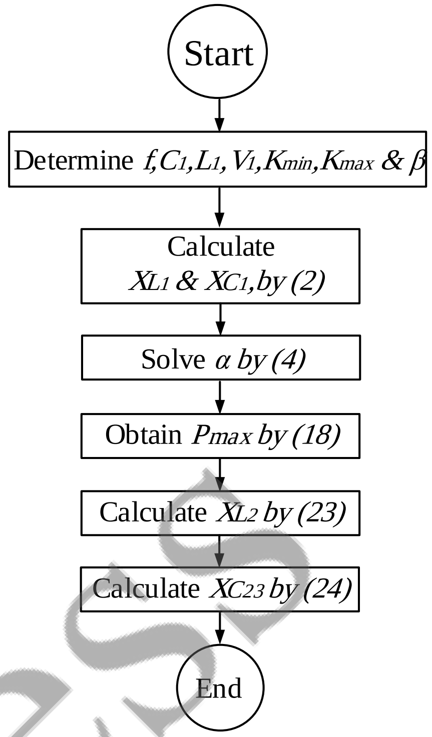

Fig. 7 Flow chart for calculating design parameters.

2.4 Circuit parameter design

To increase misalignment tolerance and maintain stable output power with minimal fluctuation, the circuit parameters are carefully designed and optimized. In this structure, the parameters are chosen to cover the full range of the coupling coefficient, from k_{min} to k_{max}. Therefore, the determination of circuit parameters depends on the values of k_{min1} to k_{max4}.

$$X_{L2}=\frac{2\alpha R_{L}\left(\beta-2\sqrt{\beta}+1\right)}{\pi^{2}k_{\min}{}^{2}(1-\beta)} \tag{23}$$

After determining the value of the X_{L2} parameter, the value of X_{C23} is determined.

$$X_{C23}=\frac{k_{\max}\sqrt{2R_{L}X_{L2}(1-\beta)}}{\sqrt{\alpha\pi^{2}\left(\beta+2\sqrt{\beta}+1\right)}} \tag{24}$$

Notably, the values of α, β, k_{min}, k_{max}, and R_L are fixed and predetermined. Fig. 7 presents the flow chart for calculating the design parameters of the proposed IPT structure.

2.5 Switching pattern

The upper regions of the four *P-k* curves are color-coded as follows: green for the *S-S-HB* mode, red for the *S-LCL-FB* mode, blue for the *S-S-FB* mode, and black for the *S-LCL-HB* mode.

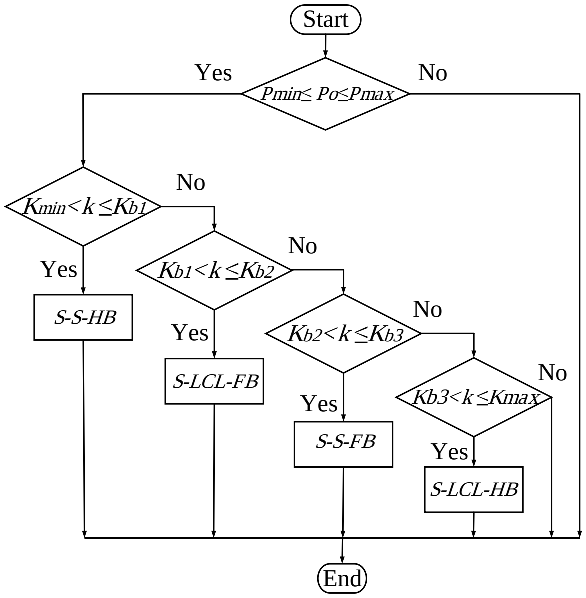

Fig. 8 switching pattern of the proposed detuned IPT.

When k is in the range of $k_{min1}<k<k_{b1}$, S-*S-HB* mode is used; if k exceeds k_{b1}, i.e., is in the range of $k_{b1}<k<k_{b2}$, *S-S-HB* mode is turned off and *S-LCL-FB* mode is turned on; if the coupling coefficient exceeds k_{b2} slow and is in the range of $k_{b2}< k < k_{b3}$, *S-S-FB* mode is switched; and finally, if the coupling factor k increases from k_{b3}, that is, it is in the range of $k_{b3}<k<k_{min4}$, *S-LCL-HB* mode is employed. The noteworthy point is that in the four working modes, the output power should be in the range of $P_{min}<P_o<P_{max}$, otherwise the proposed IPT structure should be turned off. The switching flowchart of the proposed IPT structure is shown in Fig. 8.

3 Simulation results

To verify the validity of the theoretical analysis and confirm the performance of the proposed structure, it has been simulated in MATLAB. The parameters of the primary and secondary compensation networks are considered in such a way that the output power is 400 W with a power fluctuation of 3%. Table 1 shows the parameters of the proposed structure.

The *P-k* curve of all four modes of the proposed IPT structure is shown in Fig. 9.

Table 1 Simulation parameters

Parameter	Value	Parameter	Value
f	250 kHz	k_{min}	0.1
L_1	38.16 µH	k_{b1}	0.14
L_2	27.65 µH	k_{b2}	0.1987
L_{21}	5.48 µH	k_{b3}	0.28
C_1	13.24 nF	k_{max}	0.4
C_{22}	12.23 nF	α	0.19
C_{21}	6.06 nF	β	0.03
C_{23}	73.80 nF	P_{max}	400 W
V_{in}	100 V	R_L	15 Ω

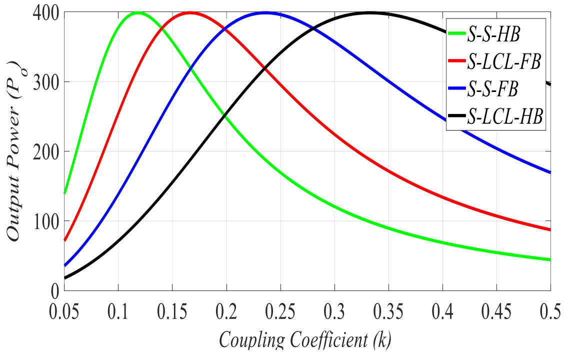

Fig.9 the *P-k* curves of the proposed detuned IPT.

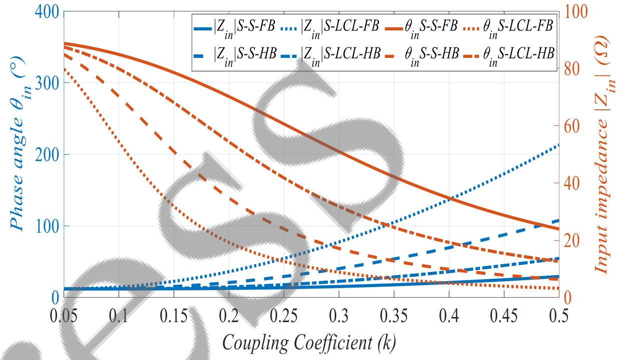

Fig.10 the input impedance and its phase angle of the proposed detuned IPT.

As illustrated in Fig. 9, the coupling coefficient range for *S-S-HB* mode is 0.1-0.14, for *S-LCL-FB* mode it is 0.14-0.1987, for *S-S-FB* mode it is 0.1987-0.28, and for *S-LCL-HB* mode it falls within 0.28-0.4. Throughout the simulation, the coupling coefficient varied from 0.1-0.4, and the simulation results are presented below.

As shown in Fig.10, the input phase angle of the inverter for *S-S-HB* mode from 72° to 54°, for *S-LCL-FB* mode from 35° to 19°, for *S-S-FB* mode from 70° to 54° and for *S-LCL-HB* mode has been reduced from 35° to 19°. The input impedance is inductive in the range of coupling factor variation from 0.1 to 0.4, which provides the ZVS condition for the inverter.

Fig. 11 displays the coupling coefficient variations against the simulation duration. It can be observed that at time intervals of 0.0-0.02 s, 0.02-0.03 s, 0.03-0.04 s, 0.04-0.05 s, 0.05-0.06 s, and 0.06-0.07 s, the coupling coefficients are 0.1, 0.15, 0.21, 0.3, 0.36, and 0.4, respectively.

Fig.12 displays the waveforms of the inverter output current/voltage and rectifier input current/voltage for the proposed IPT structure with various coupling coefficients, with a load resistance of R_L = 15 Ω. The corresponding coupling coefficients in Fig.12 (a)-(d) are 0.10, 0.15, 0.21 and 0.36, respectively.

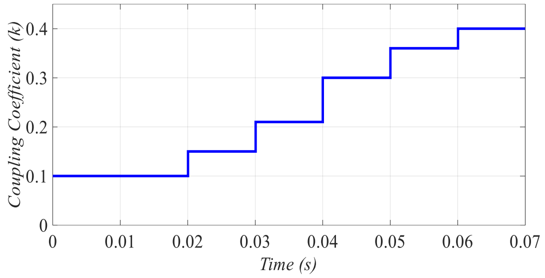

Fig. 11. The coupling coefficient variations against the simulation duration.

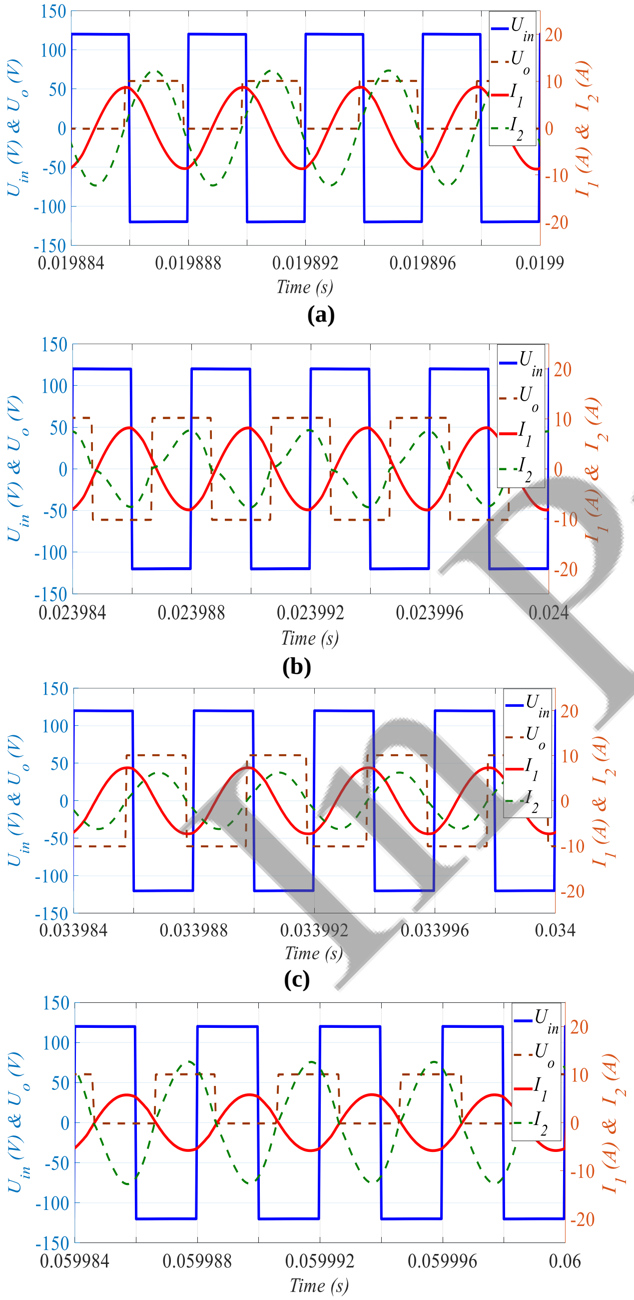

(a)

(b)

(c)

(d)

Fig. 12 Inverter input voltage/current waveforms and rectifier output voltage/current waveforms; (a) k=0.1, (b) k=0.15, (c) k=0.21, (d) k=0.36.

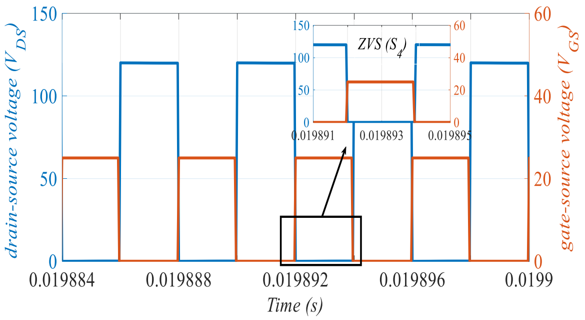

Fig. 13 the V_{GS} and V_{DS} waveforms of MOSFET S_4

It can be seen that the input impedance of the system is inductive, which is very effective to implement ZVS for high-frequency inverter.

Fig.13 illustrates the gate-source voltage (V_{GS}) and drain-source voltage (V_{DS}) waveforms of MOSFET S_4 for various coupling coefficients. It is evident that the ZVS condition is achieved for the inverter switches within the allowed coupling factor range [0.1-0.4].

3.1 Dynamic Transient between different modes

The dynamic transient waveform of the output voltage between different operating modes is shown in Fig.14 (a)-(e). It is worth noting that the output voltage has changed slowly in different modes.

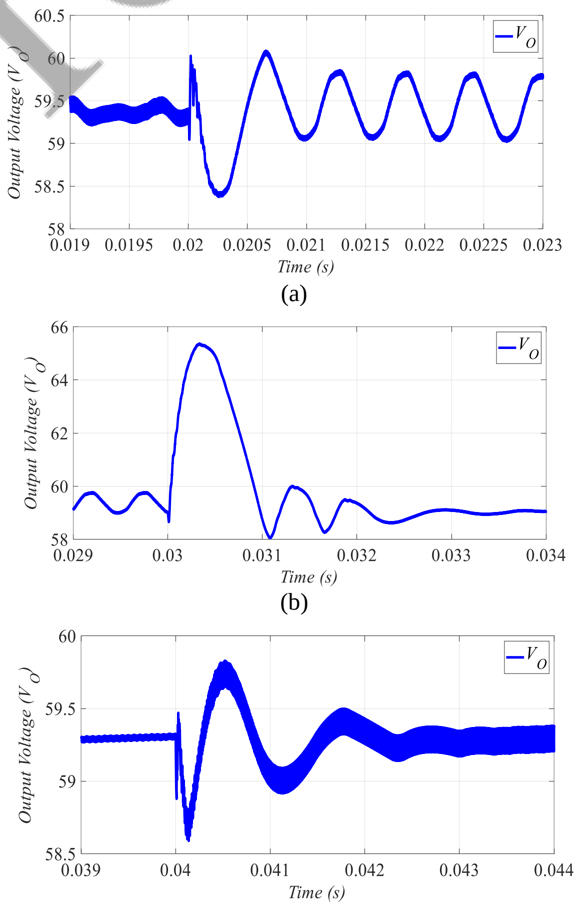

(a)

(b)

(c)

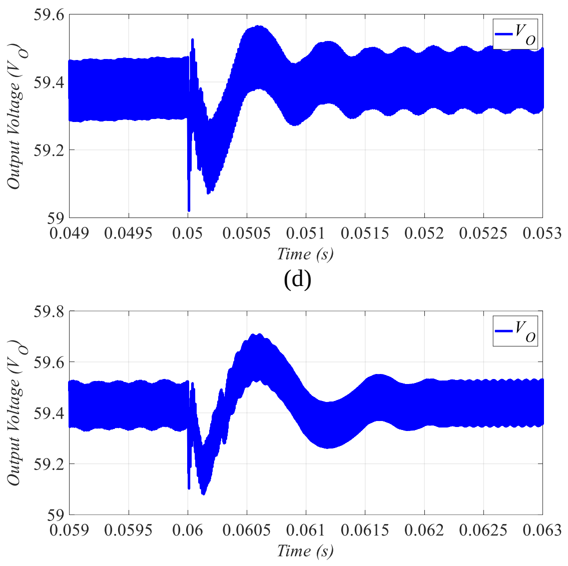

(d)

(e)

Fig. 14 Dynamic transition of V_o between modes; (a) *S-S-HB* to *S-LCL-FB* at k=0.15, (b) *S-LCL-FB* to *S-S-FB* at k=0.21, (c) *S-S-FB* to *S-LCL-HB* at k=0.3, (d) *S-LCL-HB* at k=0.36, (e) *S-LCL-HB* at k=0.4

3.1 *P-k* and efficiency -*k* curves of the proposed structure

Fig. 15 depicts the output power curve of the proposed structure versus misalignment.

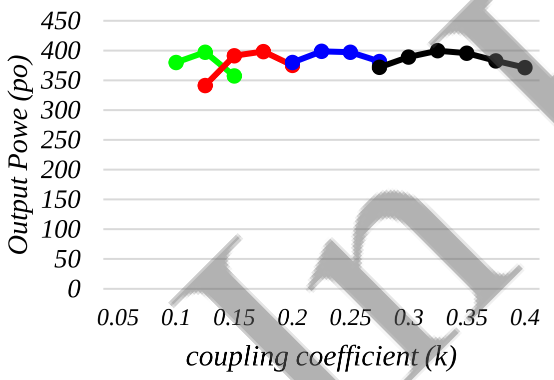

Fig. 15 Measured *P-k* curves of the IPT versus misalignment.

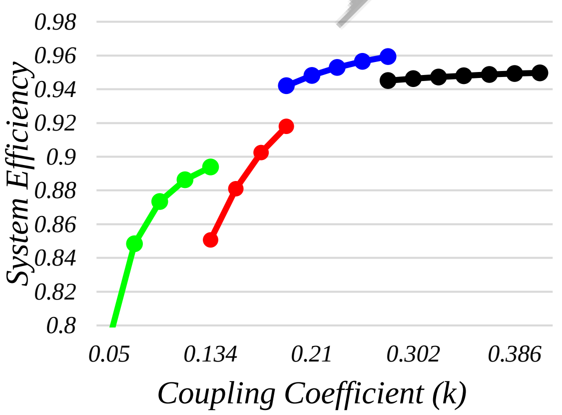

Fig. 16 Measured efficiencies of the IPT versus misalignment.

The coupling range of *S-S-HB* mode is 0.1-0.14, the coupling range of *S-S-LCL-FB* mode is 0.14-0.1987, the coupling range of *S-S-FB* mode is 0.1987-0.28, and the coupling coefficient of *S-LCL-HB* mode is in the range of 0.28-0.4. P_{max} and P_{min} are about 400 W and 377 W, respectively, with a power fluctuation of about 3%. Therefore, the proposed structure, exhibiting the lowest power fluctuation, demonstrates remarkable resistance to misalignment, contributing to enhanced system performance.

Fig. 16 illustrates the overall efficiency of the dc-dc system in the proposed structure against misalignment. The minimum and maximum efficiency within the coupling factor range [0.1-0.4] are 80% and 95.9%, respectively.

4 Discussion and Comparison

Compared to other methods, the proposed structure does not require special coil design, clamp circuit design, or complex control, and it can achieve relatively stable output power against misalignment. Detailed comparison results are provided in Table 2. Compared to all methods [12], [16]-[18], [21], [22], [23]-[27], [29], [38], and [39], the proposed method demonstrates the lowest output power fluctuation, at only 3%, and accommodates the widest range of coupling variation, from 0.1 to 0.4.

Additionally, when compared to methods [18]-[20], [28]-[29], the system efficiency of this approach is comparable and acceptable, and it surpasses that of [26] and [27]. It should be noted that, compared to [21], [38] and [39] the proposed structure does not require special coil design, clamp circuit design, and complex control. Therefore, the main goal of the proposed method is to achieve maximum power transmission and relatively high efficiency against high misalignment, which is significantly superior to other methods.

Due to changes in the relative positions of the coils, the coupling coefficient is uncertain. Therefore, it should be possible to calculate the coupling factor or mutual inductance using certain system voltages or currents; mutual inductance can be estimated from either primary or secondary side information. Consequently, one of the limitations and challenges of the proposed method, compared to methods [21]-[24], [27] and [28], is the need for accurate online estimation of the coupling coefficient.

5 Conclusion

This paper proposed an IPT system based on impedance matching networks and a semi-symmetric active rectifier to tolerate a wide range of coupling factor variations. Two secondary compensation networks, controlled by two relays, create two *P-k* curves that

Table 2. Comparison with other methods proposed in the papers.

Ref.	Coil complexity	# Coil/ # Inductor	# Capacitor/ # relay	# Diode/ # Switch	*k* variations	*k* *estimation*	β	Output	*Efficiency*	P_{max}
[38]	High	3/0	3/1	8/4	0.1-0.4	High	5.98%	CP	86.1%-94.3%	400 W
[39]	High	3/0	3/1	8/4	0.14-0.39	High	4.4%	CP	83.2%-93.5%	480 W
[27]	Low	2/1	3/1	4/4	0.1-0.25	Low	4.4%	CP	85.6%-97.1%	400 W
[26]	Low	2/0	3/0	4/4	0.21-0.36	Low	10.6%	CP/CV	86%-94.8%	300 W
[25]	Low	2/1	3/0	4/4	0.16-0.32	High	20%	CP	88.5%-92.6%	450 w
[24]	Low	2/0	2/0	4/4	0.08-0.2	Low	11.1%	CP	66%-73%	70 W
[23]	Low	2/2	3/0	4/4	0.14-0.28	Low	20%	CP	83.5%-87.5%	90 W
[12]	High	3/2	4/0	4/4	0.14-0.29	Low	5%	CC	92.1%-93.1%	3400W
[17]	High	4/0	6/0	4/4	0.15-0.35	High	5%	CP	85%-94%	3300W
[16]	High	4/2	6/0	4/4	0.1-0.25	High	10%	CV	88%-93%	3500W
[21]	High	4/4	8/2	4/4	0.1-0.26	Low	10%	CC/CV	75.1%-93.9%	1000W
[22]	High	4/1	5/0	4/4	0.09-0.26	Low	10%	CV	87%-93%	3000W
[29]	Low	2/1	2/1	4/4	0.1-0.4	High	17.5%	CP	87.5%-95.6%	400 W
This work	Low	2/1	4/2	3/5	0.1-0.4	High	3%	CP/CV	80%-95.9%	400 W

enable the system to switch between modes. The two *P-k* curves are shifted to the left and right by the semi-symmetric active rectifier in *FB* and *HB* modes. As a result, four *P-k* curves with highly stable operating regions are created, expanding the range of the coupling coefficient. With the appropriate algorithm for switching between different operational regions, the system can achieve maximum efficiency and stable power transfer, exhibiting very low fluctuations against wide range coupling variations. The simulation results show that for 400% changes in coupling coefficient (0.1–0.4), the output power fluctuation rate of the proposed structure is only 3%, and the efficiency varies from 80% to 95.9%. Simulation results compared to other methods show very good performance against significant misalignment tolerance and efficiency improvement, which is suitable for battery charging systems under constant power (CP) and constant voltage (CV) modes. The proposed IPT system does not require complex control, dedicated coil design, and clamp circuit.

Intellectual Property

The authors declare that the method described in this manuscript has been protected under intellectual property law. The work has been patented under the title "Inductive Power Transfer system with the ability to maintain stable transmission power and improve efficiency with a tolerance approach against a wide range of misalignment," Patent No. 111932, issued by the Iran Intellectual Property Office, in 2024 [40].

References

[1] J. T. Boys and G. A. Covic, "The inductive power transfer story at the University of Auckland," *IEEE circuits and systems magazine*, vol. 15, no. 2, pp. 6-27, 2015.

[2] S. Zhou and C. C. Mi, "Multi-paralleled LCC reactive power compensation networks and their tuning method for electric vehicle dynamic wireless charging," *IEEE Transactions on Industrial Electronics*, vol. 63, no. 10, pp. 6546-6556, 2015.

[3] M. G. Eftekhar, Z. Ouyang, M. A. Andersen, P. B. Andersen, L. A. d. S. Ribeiro, and E. Schaltz, "Efficiency study of vertical distance variations in wireless power transfer for e-mobility," *IEEE Transactions on Magnetics*, vol. 52, no. 7, pp. 1-4, 2016.

[4] Y. Li, R. Mai, L. Lu, and Z. He, "Active and reactive currents decomposition-based control of angle and magnitude of current for a parallel multiinverter IPT system," *IEEE Transactions on Power Electronics*, vol. 32, no. 2, pp. 1602-1614, 2016.

[5] K. V. T. Piipponen, R. Sepponen, and P. Eskelinen, "A biosignal instrumentation system using capacitive coupling for power and signal isolation," *IEEE Transactions on Biomedical Engineering*, vol. 54, no. 10, pp. 1822-1828, 2007.

[6] S. Hui, "Planar wireless charging technology for portable electronic products and Qi," *Proceedings of the IEEE*, vol. 101, no. 6, pp. 1290-1301, 2013.

[7] S. Lee, B. Choi, and C. T. Rim, "Dynamics characterization of the inductive power transfer system for online electric vehicles by Laplace phasor transform," *IEEE Transactions on Power Electronics*, vol. 28, no. 12, pp. 5902-5909, 2013.

[8] K. Song *et al.*, "Design of DD coil with high misalignment tolerance and low EMF emissions for wireless electric vehicle charging systems," *IEEE Transactions on Power Electronics*, vol. 35, no. 9, pp. 9034-9045, 2020.

[9] G. Yang *et al.*, "Interoperability improvement for rectangular pad and DD pad of wireless electric

vehicle charging system based on adaptive position adjustment," *IEEE Transactions on Industry Applications*, vol. 57, no. 3, pp. 2613-2624, 2021.

[10] A. Zaheer, H. Hao, G. A. Covic, and D. Kacprzak, "Investigation of multiple decoupled coil primary pad topologies in lumped IPT systems for interoperable electric vehicle charging," *IEEE Transactions on Power Electronics*, vol. 30, no. 4, pp. 1937-1955, 2014.

[11] S. Kim, G. A. Covic, and J. T. Boys, "Tripolar pad for inductive power transfer systems for EV charging," *IEEE Transactions on Power Electronics*, vol. 32, no. 7, pp. 5045-5057, 2016.

[12] Y. Chen, R. Mai, Y. Zhang, M. Li, and Z. He, "Improving misalignment tolerance for IPT system using a third-coil," *IEEE Transactions on Power Electronics*, vol. 34, no. 4, pp. 3009-3013, 2018.

[13] Y. Yao, Y. Wang, X. Liu, Y. Pei, and D. Xu, "A novel unsymmetrical coupling structure based on concentrated magnetic flux for high-misalignment IPT applications," *IEEE Transactions on Power Electronics*, vol. 34, no. 4, pp. 3110-3123, 2018.

[14] J. Mai, Y. Wang, Y. Yao, M. Sun, and D. Xu, "High-misalignment-tolerant IPT systems with solenoid and double D pads," *IEEE Transactions on Industrial Electronics*, vol. 69, no. 4, pp. 3527-3535, 2021.

[15] Y. Zhang, S. Chen, X. Li, and Y. Tang, "Design methodology of free-positioning nonoverlapping wireless charging for consumer electronics based on antiparallel windings," *IEEE Transactions on Industrial Electronics*, vol. 69, no. 1, pp. 825-834, 2021.

[16] X. Qu, Y. Yao, D. Wang, S.-C. Wong, and K. T. Chi, "A family of hybrid IPT topologies with near load-independent output and high tolerance to pad misalignment," *IEEE Transactions on Power Electronics*, vol. 35, no. 7, pp. 6867-6877, 2019.

[17] L. Zhao, D. J. Thrimawithana, U. K. Madawala, A. P. Hu, and C. C. Mi, "A misalignment-tolerant series-hybrid wireless EV charging system with integrated magnetics," *IEEE Transactions on Power Electronics*, vol. 34, no. 2, pp. 1276-1285, 2018.

[18] Y. Chen *et al.*, "A hybrid inductive power transfer system with misalignment tolerance using quadruple-D quadrature pads," *IEEE Transactions on Power Electronics*, vol. 35, no. 6, pp. 6039-6049, 2019.

[19] R. Mai, B. Yang, Y. Chen, N. Yang, Z. He, and S. Gao, "A misalignment tolerant IPT system with intermediate coils for constant-current output," *IEEE Transactions on Power Electronics*, vol. 34, no. 8, pp. 7151-7155, 2019.

[20] L. Zhao, D. J. Thrimawithana, and U. K. Madawala, "Hybrid bidirectional wireless EV charging system tolerant to pad misalignment," *IEEE Transactions on Industrial Electronics*, vol. 64, no. 9, pp. 7079-7086, 2017.

[21] Y. Chen, B. Yang, Z. Kou, Z. He, G. Cao, and R. Mai, "Hybrid and reconfigurable IPT systems with high-misalignment tolerance for constant-current and constant-voltage battery charging," *IEEE Transactions on Power Electronics*, vol. 33, no. 10, pp. 8259-8269, 2018.

[22] W. Zhao, X. Qu, J. Lian, and K. T. Chi, "A family of hybrid IPT couplers with high tolerance to pad misalignment," *IEEE Transactions on Power Electronics*, vol. 37, no. 3, pp. 3617-3625, 2021.

[23] H. Feng, A. Dayerizadeh, and S. M. Lukic, "A coupling-insensitive X-type IPT system for high position tolerance," *IEEE Transactions on Industrial Electronics*, vol. 68, no. 8, pp. 6917-6926, 2020.

[24] H. Feng, T. Cai, S. Duan, X. Zhang, H. Hu, and J. Niu, "A dual-side-detuned series–series compensated resonant converter for wide charging region in a wireless power transfer system," *IEEE Transactions on Industrial Electronics*, vol. 65, no. 3, pp. 2177-2188, 2017.

[25] H. Feng, T. Cai, S. Duan, J. Zhao, X. Zhang, and C. Chen, "An LCC-compensated resonant converter optimized for robust reaction to large coupling variation in dynamic wireless power transfer," *IEEE Transactions on Industrial Electronics*, vol. 63, no. 10, pp. 6591-6601, 2016.

[26] J. Mai, Y. Wang, Y. Yao, and D. Xu, "Analysis and design of high-misalignment-tolerant compensation topologies with constant-current or constant-voltage output for IPT systems," *IEEE Transactions on Power Electronics*, vol. 36, no. 3, pp. 2685-2695, 2020.

[27] Y. Chen *et al.*, "Reconfigurable topology for IPT system maintaining stable transmission power over large coupling variation," *IEEE Transactions on Power Electronics*, vol. 35, no. 5, pp. 4915-4924, 2019.

[28] Y. Zhang *et al.*, "Misalignment-tolerant dual-transmitter electric vehicle wireless charging system with reconfigurable topologies," *IEEE Transactions on Power Electronics*, vol. 37, no. 8, pp. 8816-8819, 2022.

[29] Y. Chen, S. He, B. Yang, S. Chen, Z. He, and R. Mai, "Reconfigurable rectifier-based detuned series-series compensated IPT system for anti-misalignment and efficiency improvement," *IEEE Transactions on Power Electronics*, vol. 38, no. 2, pp. 2720-2729, 2022.

[30] J. M. Miller, O. C. Onar, and M. Chinthavali, "Primary-side power flow control of wireless power transfer for electric vehicle charging," *IEEE*

journal of Emerging and selected topics in power electronics, vol. 3, no. 1, pp. 147-162, 2014.

[31] Z. Zhang, F. Zhu, D. Xu, P. T. Krein, and H. Ma, "An integrated inductive power transfer system design with a variable inductor for misalignment tolerance and battery charging applications," *IEEE Transactions on Power Electronics*, vol. 35, no. 11, pp. 11544-11556, 2020.

[32] Z. Li, H. Liu, Y. Huo, J. He, Y. Tian, and J. Liu, "High-misalignment tolerance wireless charging system for constant power output using dual transmission channels with magnetic flux controlled inductors," *IEEE Transactions on Power Electronics*, vol. 37, no. 11, pp. 13930-13945, 2022.

[33] D. Thenathayalan and J.-H. Park, "Highly flexible high-efficiency multiple-resonant wireless power transfer system using a controllable inductor," *IEEE Journal of Emerging and Selected Topics in Power Electronics,* vol. 7, no. 3, pp. 1914-1930, 2018.

[34] H.-C. Hsieh and J.-S. Lai, "A half-bridge CLC-series wireless power transfer system with clamping diodes," in *2021 IEEE International Future Energy Electronics Conference (IFEEC)*, 2021: IEEE, pp. 1-6.

[35] Z. Huang, G. Wang, J. Yu, and X. Qu, "A novel clamp coil assisted IPT battery charger with inherent CC-to-CV transition capability," *IEEE Transactions on Power Electronics*, vol. 36, no. 8, pp. 8607-8611, 2021.

[36] P. Cao *et al.*, "An IPT system with constant current and constant voltage output features for EV charging," in *IECON 2018-44th Annual Conference of the IEEE Industrial Electronics Society*, 2018: IEEE, pp. 4775-4780.

[37] R. Mai, Y. Liu, Y. Li, P. Yue, G. Cao, and Z. He, "An active-rectifier-based maximum efficiency tracking method using an additional measurement coil for wireless power transfer," *IEEE Transactions on Power Electronics*, vol. 33, no. 1, pp. 716-728, 2017.

[38] Y. Chen *et al.*, "A clamp circuit-based inductive power transfer system with reconfigurable rectifier tolerating extensive coupling variations," *IEEE Transactions on Power Electronics*, 2023.

[39] B. Yang *et al.*, "A clamped IPT system with adaptive mode switching against large coupling variations," *IEEE Transactions on Power Electronics*, 2023.

[40] Jalalian Ebrahimi, M., Shamsi-Nejad, M.A. "Inductive Power Transfer system with the ability to maintain stable transmission power and improve efficiency with a tolerance approach against a wide range of misalignment." Patent No. 111932, *Iran Intellectual Property Office*, 2024.

Mostafa Jalalian Ebrahimi was born in Mashhad, Iran, in 1989. He received his B.Sc. degree in Electrical Power Engineering from the Mashhad Institute of Technology, Mashhad, Iran, in 2012; and his M.Sc. degree from the K. N. Toosi University of Technology, Tehran, Iran, in 2015. He is currently working toward the Ph.D. degree in the Faculty of Electrical Engineering at the University of Birjand, Iran.

His current research interests include inductive power transfer, misalignment tolerance improvement, electric vehicles charging, and design and control of power electronic converters.

M. A. Shamsi-Nejad received the B.Sc. degree in Electrical Engineering and the M.Sc. degree from the Sharif University of Technology, Tehran, Iran, in 1990 and 1996, respectively, and the Ph.D. degree from the Institut National Polytechnique de Lorraine (INPL), Nancy, France, in 2006. He is currently a Professor at the University of Birjand, Iran.

His research interests include Birjand University deal with control of electrical machines, renewable energies, and power electronics.